J Mater Sci: Mater Electron (2017) 28:588–594
DOI 10.1007/s10854-016-5562-6

Improvement in the sintering process of $Ba_{0.85}Ca_{0.15}Zr_{0.1}Ti_{0.9}O_3$ ceramics by the replacement of Zr by Hf

A. Di Loreto[1,2] · R. Machado[1] · A. Frattini[1,2] · M. G. Stachiotti[1]

Received: 23 June 2016 / Accepted: 16 August 2016 / Published online: 20 August 2016

Abstract We investigate the effects of replacing Zr^{4+} ions by Hf^{4+} on the sintering and electrical properties of $Ba_{0.85}Ca_{0.15}Zr_{0.1}Ti_{0.9}O_3$ (BCZT) lead-free piezoceramics. For that purpose, $Ba_{0.85}Ca_{0.15}Hf_{0.1}Ti_{0.9}O_3$ ceramics were sintered at different temperatures and their properties were compared to those of BCZT fabricated under the same conditions. We show that Hf as B-site dopant facilitates the formation of the perovskite phase during the calcination process and improves the electrical properties of the ceramics due to the development of a denser microstructure with greater grain size and lower porosity.

1 Introduction

The development of lead-free piezoelectric ceramics has received recently considerable attention from the environmental protection point of view [1–6]. A way to enhance the piezoelectric response of lead-free materials is the compositional engineering approach, where the composition of the compound is optimized by bringing it to the vicinity of a structural instability [7]. It is well known that the phase transition temperatures of $BaTiO_3$ (BTO) can be altered by doping with either A or/and B site substitutions. For instance, the replacement of Ba^{2+} by Ca^{2+} does not strongly affect the Curie temperature, but significantly lowers the T-O and O-R transition temperatures [8, 9]. A different behavior is observed for Zr^{4+} at the B site, where the three transition temperatures of BTO move closer with increasing Zr content and merge near room temperature for the $x = 0.15$ composition [10, 11]. The combination of these two effects generates a triple point on the morphotropic phase boundary in $xBa(Zr_{0.2}Ti_{0.8})O_3$-$[1 - x](Ba_{0.7}Ca_{0.3})TiO_3$ solid solutions [12, 13]. For this reason, these compounds have attracted great attention, particularly for the composition $x = 0.5$ ($Ba_{0.85}Ca_{0.15}Zr_{0.1}Ti_{0.9}O_3$, for short BCZT) which displays piezoelectric properties comparable to those of $PbZr_xTi_{1-x}O_3$ at room temperature [14, 15].

A number of existing applications emerge, where the usage of lead-free piezoceramics may be envisaged in the near future [6, 16]. One important drawback of BCZT ceramics is however the high synthesis (~1300 °C) and sintering (~1450 °C) temperatures. Sintering BCZT ceramics at lower temperatures is a difficult task and many researchers have devoted to improving the temperature processing by tailoring the sintering conditions. For instance, the addition of a small amount of suitable materials is a traditional method used to enhance densification in ceramics, and sintering aids like CeO_2 [17], MnO_2 [18], Dy_2O_3 [19] and $Ba(Cu_{0.5}W_{0.5})O_3$ [20] have been tested for BCZT. In this work we show that the replacement of Zr by Hf is a simple and effective strategy to improve the sinterability of BCZT ceramics without the need of foreign additives. We show that the use of Hf facilitates the formation of the perovskite phase during the calcination process and improves the electrical properties of the ceramics.

2 Experimental procedure

BCHT and BCZT powders were synthesized from a mixture of $BaCO_3$, $CaCO_3$, and HfO_2, ZrO_2 and TiO_2 by a milling process using a planetary ball mill equipment

✉ M. G. Stachiotti
stachiotti@ifir-conicet.gov.ar

[1] Instituto de Física Rosario, Universidad Nacional de Rosario-CONICET, 27 de Febrero 210 Bis, 2000 Rosario, Argentina

[2] Área Física, Dpto. de Química Física, FCByF, Universidad Nacional de Rosario, 2000 Rosario, Argentina

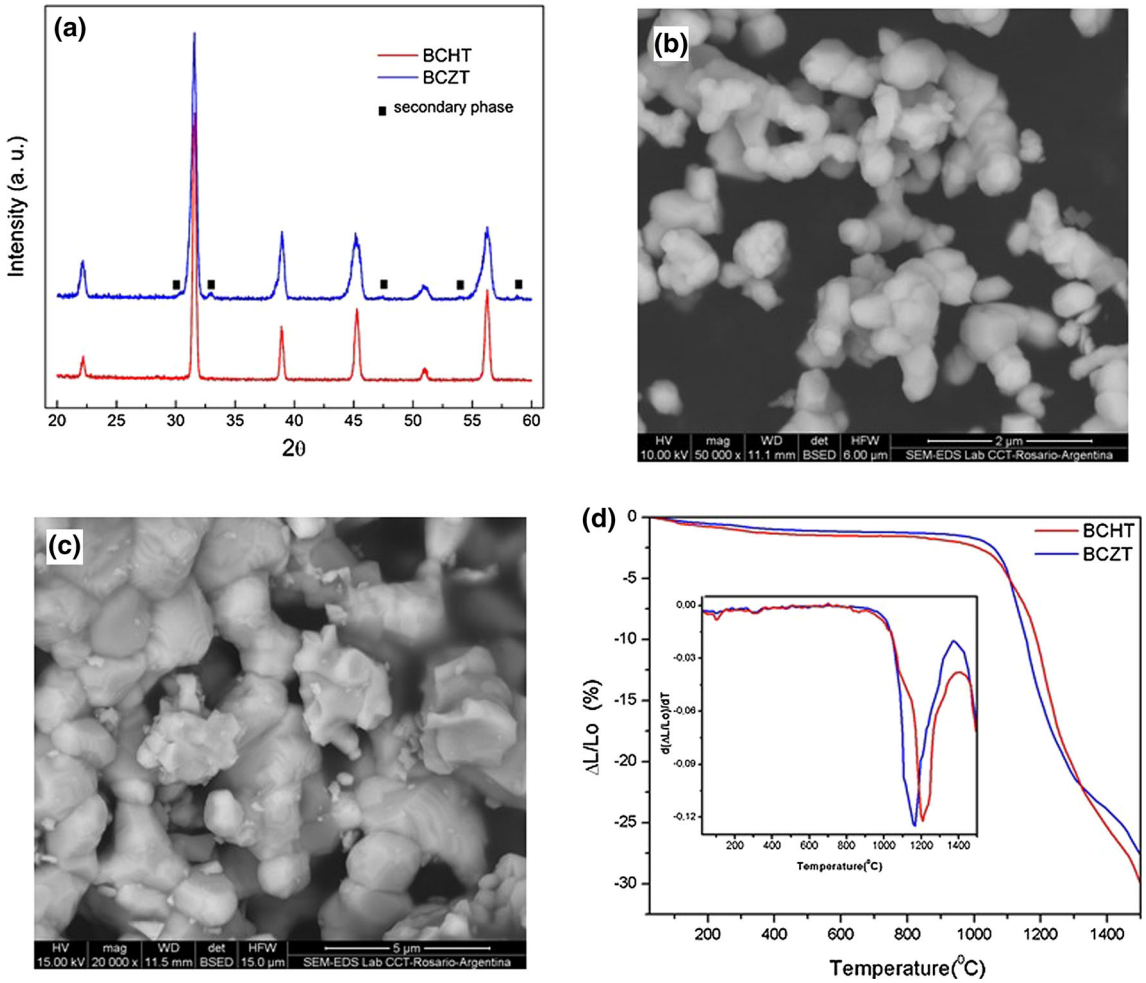

Fig. 1 **a** XRD patterns of powders calcined at 1250 °C for 4 h. **b** SEM image of the BCZT calcined powder. **c** SEM image of the BCHT calcined powder. **d** Dilatometric curves of powders calcined at 1250 °C. The *inset* compares the temperature dependence of shrinkage rate of two samples

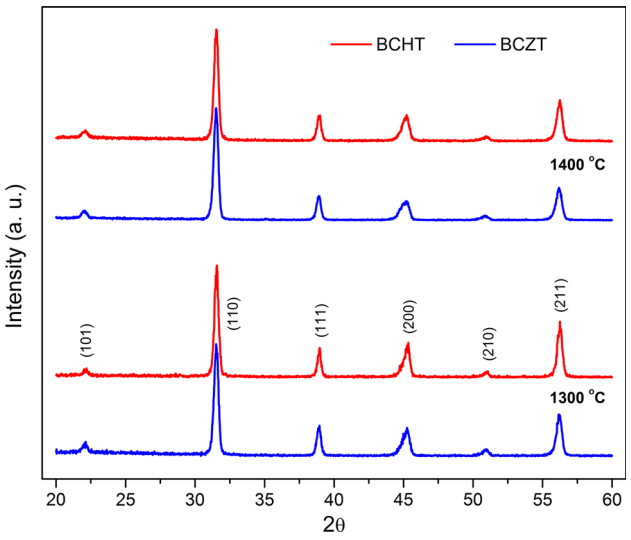

Fig. 2 XRD patterns of BCHT and BCZT ceramics sintered at 1300 °C (*bottom*) and 1400 °C (*top*)

(Torrey Hills Technologies ND 0.4 L). The carbonates are hygroscopic materials and hence due care was taken in their handling during the material formation. The precursor powders were initially dried at 230 °C for 4 h to remove the absorbed moisture, and then they were weighed based on the stoichiometric formula and milled for 12 h. The milled powder was calcined at 1250 °C for 4 h. After that, they were ball milled again for 12 h. The whole ball milling process was done with agate ball media. The obtained powders were mixed with a polyvinyl butyral (PVB) binder solution and then die-pressed into disks with dimensions of Ø10 mm × 2 mm. The pellets were sintered at two different temperatures (1300 and 1400 °C) for 2 h. The density of the ceramic samples was measured by the Archimedes' method. The theoretical densities, calculated using the lattice parameters obtained by the refinement of the X-ray patterns, are 5.94 g/cm^3 for BCHT and 5.72 g/cm^3 for BCZT.

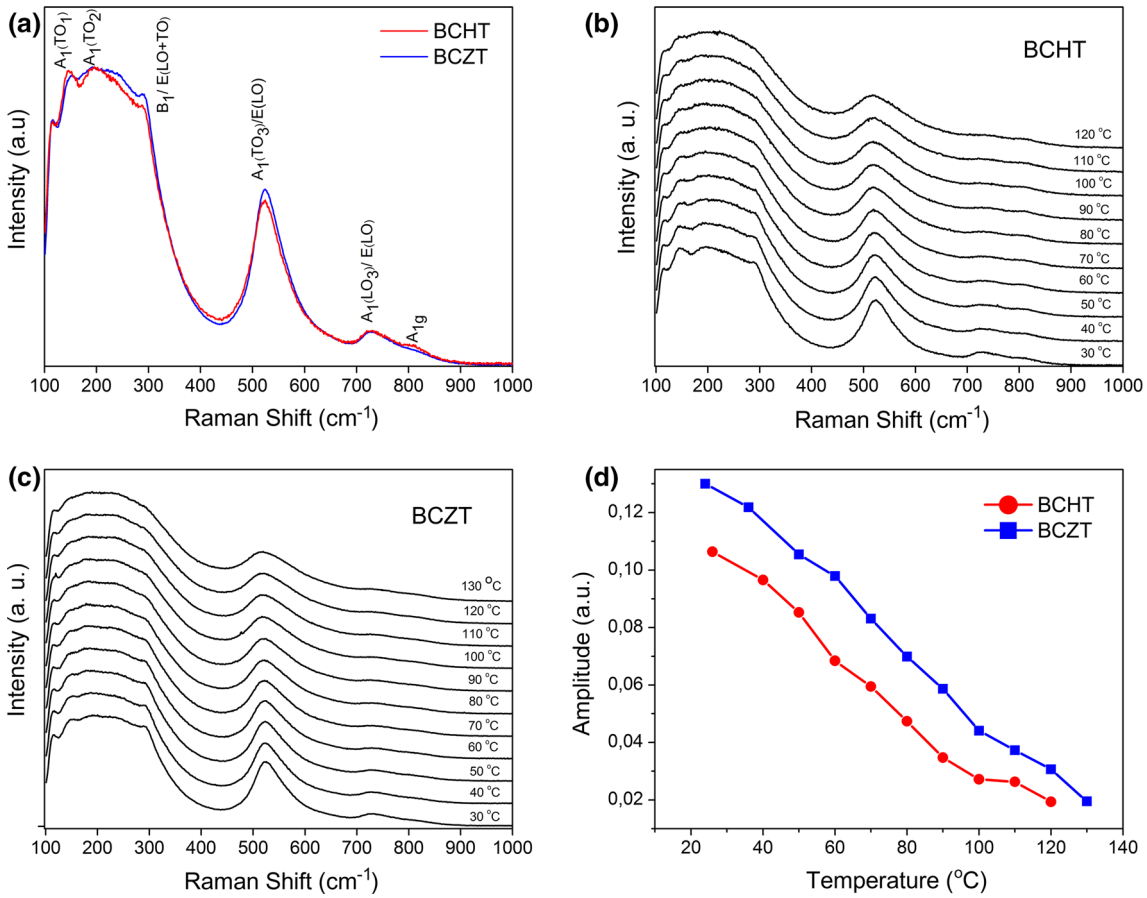

Fig. 3 Raman spectra of ceramics sintered at 1400 °C. **a** Comparison of the room temperature Raman spectra of the two ceramics. **b** Thermal evolution of the Raman spectrum of BCHT. **c** Thermal evolution of the Raman spectrum of BCZT. **d** Intensities of the B1 mode as a function of temperature

Crystal structure was analyzed by X-ray diffraction (XRD) using a Philips X'Pert Pro X-ray diffractometer. Raman spectra were acquired with a Renishaw in Via Raman spectrometer by means of the 514 nm Ar-ion laser line (10 mW nominal power). The microstructure of the samples was examined by Scanning Electron Microscopy (SEM) using a FEI Quanta 200 FESEM Environmental. For electrical studies, silver electrodes were sputtered on both sides of the samples. The temperature dependence of the dielectric properties of the ceramics was measured using an LCR meter (QuadTech 7600 plus) attached to a programmable furnace. The piezoelectric constant d_{33} was measured by a Berlincourt-type d_{33} m (KCF technologies, model PM3001).

3 Results and discussion

The two materials display differences in the formation process of the perovskite phase. Figure 1a shows X-ray patterns of powders prepared by mixing the starting chemicals (without an intense milling) followed by calcination at 1250 °C for 4 h. While the spectrum for BCZT presents additional peaks at ~30°, 33°, 47.5°, 54° and 59°, secondary phases are not detected for BCHT indicating that Hf as B-site dopant facilitates the formation of perovskite phase. Even more, the diffraction peaks for BCHT are narrower than those of BCZT suggesting better crystallization and greater particle size. To support this point we show in Fig. 1 SEM images of the calcined powders. While the BCZT powder consists of particles with sizes less than 1 μm (Fig. 1b), the average crystallite size for BCHT is considerably greater and the particles are strongly bonded by the formation of sintering necks (Fig. 1c). To compare the densification processes of the two materials, we show in Fig. 1d the dilatometry curves for pellets prepared from powders calcined at 1250 °C and milled for 12 h. The densification takes place at temperatures >1100 °C, showing local maximums of densification rate at 1210 °C for BCHT and 1170 °C for BCZT. However, the two curves intersect each other at ~1300 °C, indicating that the shrinkage in BCHT is higher than in BCZT above that temperature. Such a shrinkage behavior suggests that hafnium

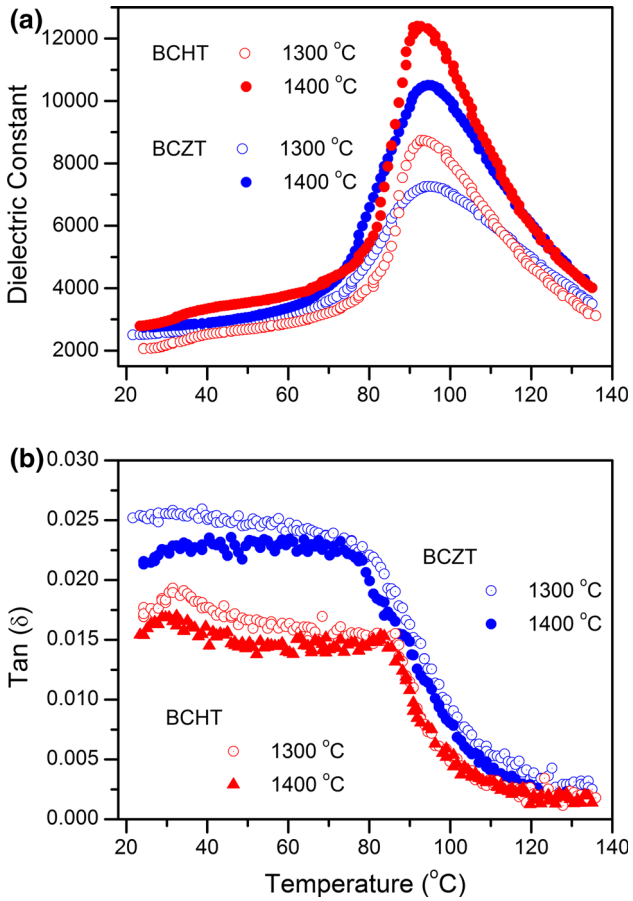

Fig. 4 **a** Temperature dependence of the dielectric constant of BCHT and BCZT ceramics sintered at 1300 and 1400 °C. The data were taken at 10 kHz during the heating process of the thermal cycle. **b** Temperature dependence of the dielectric losses

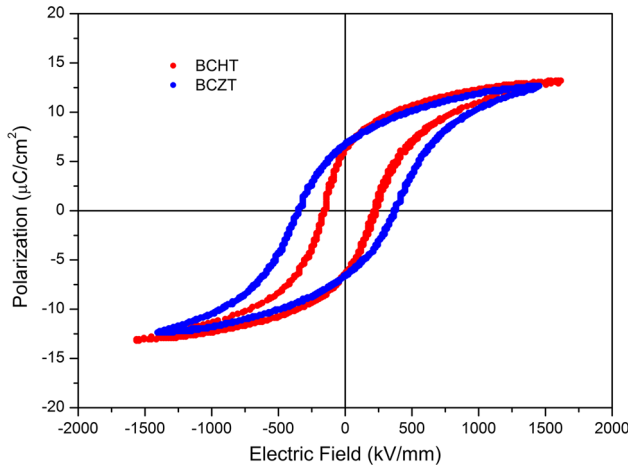

Fig. 5 Polarization hysteresis loops of BCHT and BCZT ceramics annealed at 1400 °C. The cycles were measured at 50 Hz

as B-site dopant enhances densification in samples sintered above 1300 °C.

Figure 2 shows X-ray diffraction patterns of ceramics sintered at 1300 °C and 1400 °C. Secondary phases are not detected in the spectra. We observe practically no difference in the position of the diffraction peaks, which indicates that the replacement of Zr by Hf practically does not affect the lattice constants. Structural properties at local scale were investigated by Raman spectroscopy analyses. Figure 3a compares the room-temperature Raman spectra of BCHT and BCZT ceramics sintered at 1400 °C. Both spectra look quite similar, sharing close similarities to those of BTO [21–23]. The phonon mode assignment corresponds to the tetragonal symmetry of BTO, for which phonon modes are decomposed into eight branches at the Γ-point: $\Gamma = 3A_1 + 4\,E + 1\,B_1$ [24]. Phonon frequencies were obtained by the deconvolution of vibration modes using Lorentzian functions. After least-squares refinements the resulting frequencies are: 111, 133, 168, 231, 294, 521, 533 and 749 cm^{-1} for BCHT and 112, 132, 164, 227, 295, 519, 532 and 747 cm^{-1} for BCZT. It is clear that the two sets of frequencies are very similar. We note that similar frequencies were obtained from first-principles calculations of Γ-point phonons in $BaZrO_3$ and $BaHfO_3$ [25]. Figure 3b, c show the evolution of the Raman spectra with temperature. As is common in BTO-based ceramics, there is a finer structure that shows signatures of phase transitions. In our case, those are seen as weak features at ∼160 and ∼300 cm^{-1}, and the transition from the tetragonal to the cubic phase can be inferred from the loss of the intensity of those vibrational lines at ∼100 °C. To analyze the thermal behavior more precisely, the B_1 mode at ∼300 cm^{-1} has been fitted at different temperatures to provide the temperature-dependent amplitude data shown in Fig. 3d. A signature of the phase transition is clearly seen in the loss of the intensity of this vibrational line. Although we cannot determine the transition temperatures exactly (in BCZT ceramics the intensity of vibrational lines are still seen at temperatures above Tc [26]), Fig. 3d indicates that the replacement of Zr by Hf practically does not affect the Curie temperature. In summary, both the crystal structure and the vibrational properties of BCHT and BCZT are very similar. This can be understood from the great similarity in both, the chemical properties (Hf is below Zr in the periodic table of elements) and the ionic radii ($R_{Zr}^{+4} = 86$ pm and $R_{Hf}^{+4} = 85$ pm for 6-coordinate octahedral ions). In spite of that, the differences in the sintering processes discussed above affect the microstructural development and the electrical properties of the ceramics.

Figure 4a shows the temperature dependence of the dielectric constant of BCHT and BCZT ceramics sintered at 1300 and 1400 °C. The corresponding losses are plotted in Fig. 4b. The data were taken during the heating process of the thermal cycle. Although we made measurements at different frequencies, only the data for 10 kHz are presented for the sake of clarity. The BCHT ceramics exhibit

two phase transition peaks. The first one is associated with the O–T phase transition near 35 °C. Anomalies related with this transition are also observed as small peaks in the dielectric loss. The second peak at ~94 °C corresponds to the T–C phase transition. The Curie temperature for BCZT is practically the same (~96 °C). These features are in agreement with previous studies [12, 13, 27]. We note, however, that the ferroelectric peak becomes higher and narrower when Hf replaces Zr, what is an indication of a different grain size [14]. Another interesting point is that the dielectric losses for BCHT are lower than those for BCZT across the entire temperature and frequency range.

The room-temperature polarization hysteresis curves for ceramics annealed at 1400 °C are shown in Fig. 5. It is evident that Hf produces a noticeable reduction of the coercive field (E_c). While E_c is approximately 370 V/mm for BCZT, the replacement of Zr by Hf reduces E_c to ~200 V/mm. This feature could be related with the decrease of dielectric loss observed in the Hf-based ceramics, which indicates a decrease in the oxygen vacancy concentration. Oxygen vacancies affect domain wall motion by screening of the polarization charge producing domain wall pinning. Regarding the remnant polarization (P_r), it remains practically unchanged. The hysteresis loops for samples sintered at 1300 °C are similar, and the corresponding values for P_r and E_c are reported in Table 1. Finally, we determined the piezoelectric d_{33} coefficients using a Berlincourt-type meter. The poling of the samples was performed at room temperature by applying a DC field of 2 kV/mm for 20 min. The d_{33} values obtained for the BCHT ceramics are higher than those of BCZT: values of 260 (190) and 380 (350) pC/N are obtained for BCHT (BCZT) ceramics sintered at 1300 and 1400 °C, respectively.

The differences observed in the electrical properties can be assigned to the microstructural development of the ceramics. We present in Fig. 6 SEM images of surface morphologies of BCHT (a) and BCZT (b) samples sintered at 1400 °C. It is clear that the replacement of Zr by Hf produces a denser microstructure with greater grain size. Average grain sizes of ~10 and 6 μm are obtained for BCHT and BCZT, respectively. Even more, the grains in BCHT seem to be glued together forming a more compact tiling. The relative density of the ceramics supports this: 98.5 % for BCHT and 97.3 % for BCZT. We can attribute the increased grain growth and pore elimination in BCHT to a liquid-phase sintering process [28]. The SEM image of Fig. 6a shows the presence of liquid phase in the intergranular region of the ceramic. It is also possible to infer the presence of liquid phase from the X-ray diffraction pattern showed in Fig. 6c, where the hunchback background in the BCHT pattern indicates the presence of amorphous phase. We thus conclude that a liquid phase

Table 1 Relative density (ρ_{rel}), average grain size (AGS), piezoelectric coefficient (d_{33}), remnant polarization (P_r), and coercive field (E_c) for BCHT and BCZT ceramics sintered at 1300 and 1400 °C

Temp. (°C)	BCHT					BCZT				
	ρ_{rel} (%)	AGS (μm)	d_{33} (pC/N)	P_r (μC/cm^2)	E_c (V/mm)	ρ_{rel} (%)	AGS (μm)	d_{33} (pC/N)	P_r (μC/cm^2)	E_c (V/mm)
1300	96.3	4.2	260	5.5	220	94.5	3.2	190	5.0	375
1400	98.5	9.6	380	6.6	200	97.3	6.2	350	6.6	370

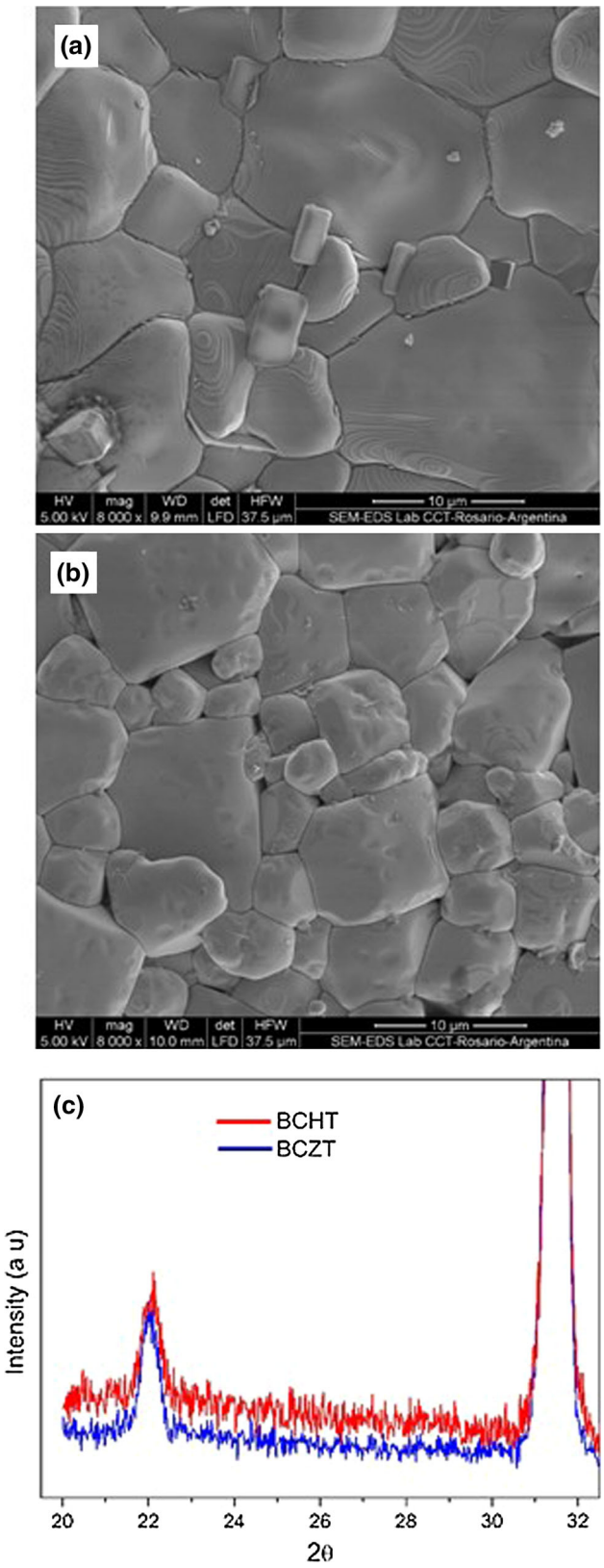

Fig. 6 SEM images showing surface morphologies of BCHT (**a**) and BCZT (**b**) ceramics annealed at 1400 °C. **c** Small-angle XRD patterns of the ceramics annealed at 1400 °C

sintering process promotes a more effective packaging of grains improving the microstructure and the electrical properties of BCHT ceramics.

4 Conclusions

$Ba_{0.85}Ca_{0.15}Hf_{0.1}Ti_{0.9}O_3$ and $Ba_{0.85}Ca_{0.15}Zr_{0.1}Ti_{0.9}O_3$ ceramics were sintered under the same conditions to compare their structural and electrical properties. We showed that both systems display similar crystal structure and vibrational properties, as expected from the close chemical similarity between Zr and Hf. In spite of that, the use of Hf as B-site dopant facilitates the sintering process of the perovskite phase and improves the electrical properties of the ceramics. In particular, the phase transition peaks become sharper, the dielectric loss and the coercive field are smaller, and the piezoelectric response increases. The improvements are due to a liquid phase sintering process that produces greater grain size and lower porosity.

Acknowledgments We thank Miriam Castro and Rodrigo Parra for their cooperation in the Raman measurements. We thank Pablo Risso for the SEM measurements. This work was sponsored by Consejo Nacional de Investigaciones Científicas y Tecnológicas (CONICET) and Agencia Nacional de Promoción Científica y Tecnológica (ANPCyT) de la República Argentina. MGS thanks support from Consejo de Investigaciones de la Universidad Nacional de Rosario (CIUNR).

References

1. T. Takenaka, H. Nagata, J. Eur. Ceram. Soc. **25**, 2693–2700 (2005)
2. P.K. Panda, J. Mater. Sci. **44**, 5049–5062 (2009)
3. J. Rödel, W. Jo, K. Seifert, E.M. Anton, T. Granzow, D. Damjanovic, J. Am. Ceram. Soc. **92**, 1153–1177 (2009)
4. Y. Lu, Y. Li, J. Adv. Dielectr. **1**, 269–288 (2011)
5. D. Xiao, J. Adv. Dielectr. **1**, 33–40 (2011)
6. J. Rödel, K. Webber, R. Dittmer, W. Jo, M. Kimura, D. Damjanovic, J. Eur. Ceram. Soc. **35**, 1659–1681 (2015)
7. S. Leontsev, R. Eitel, Sci. Technol. Adv. Mater. **11**, 044302 (2010)
8. T. Mitsui, W.B. Westphal, Phys. Rev. **124**, 1354–1359 (1961)
9. D. Fu, M. Itoh, in *Ferroelectric Materials—Synthesis and Characterization*, ed. by P. Barranco (2015). ISBN 978-953-51-2147-3
10. M. McQuarrie, F.W. Behnke, J. Am. Ceram. Soc. **37**, 539–543 (1954)
11. T. Maiti, R. Guo, A.S. Bhallaz, J. Am. Ceram. Soc. **91**, 1769–1780 (2008)
12. W.F. Liu, X.B. Ren, Phys. Rev. Lett. **103**, 257602 (2009)
13. D.S. Keeble, F. Benabdallah, P.A. Thomas, M. Maglione, J. Kreisel, Appl. Phys. Lett. **102**, 092903 (2013)
14. J.G. Hao, W.F. Bai, W. Li, J.W. Zhai, J. Am. Ceram. Soc. **95**, 1998–2006 (2012)
15. Y. Tian, X.L. Chao, L.L. Wei, P.F. Liang, Z.P. Yang, J. Appl. Phys. **113**, 184107 (2013)

16. X. Yan, K.H. Lam, X. Li, R. Chen, W. Ren, X. Ren, Q. Zhou, K.K. Shung, IEEE Trans. Ultrason. Ferroelectr. Freq. Control **60**(6), 1272 (2013)
17. Y.R. Cui, X.Y. Liu, M.H. Jiang, X.Y. Zhao, X. Shan, W.H.C.L. Yuan, C.R. Zhou, Ceram. Int. **38**, 4761 (2012)
18. A. Di Loreto, A. Frattini, R. Machado, O. de Sanctis, M.G. Stachiotti, Ferroelectrics **463**, 105–113 (2014)
19. C. Zhi-Hui, D. Jian-Ning, X. Jiu-Jun, S. Ying-Chun, Q. Jie, Q. Jian-Hua, Ferroelectrics **460**, 49–56 (2014)
20. W. Li, X. Liu, J. Ma, Y. Wu, Y. Cui, J. Mater. Sci. Mater. Electron. **24**, 1551–1555 (2013)
21. V. Sreenivas Puli, D.K. Pradhan, W. Perez, R.S. Katiyar, J. Phys. Chem. Solids **74**, 466–475 (2013)
22. V. Sreenivas Puli, A. Kumar, D.B. Chrisey, M. Tomozawa, J.F. Scott, R.S. Katiyar, J. Phys. D Appl. Phys. **44**, 395403 (2011)
23. Y.S. Seo, J.S. Ahn, I.K. Jeong, J. Korean Phys. Soc. **62**, 749–755 (2013)
24. M. Di Domenico Jr, S.H. Wemple, S.P. Porto, R.P. Bauman, Phys. Rev. **174**, 522–530 (1968)
25. R.A. Evarestov, Phys. Rev. B **83**, 014105 (2011)
26. D. Damjanovic, A. Biancoli, L. Batooli, A. Vahabzadeh, J. Trodahl, Appl. Phys. Lett. **100**, 192907 (2012)
27. C. Zhou, W.F. Liu, D.Z. Xue, X.B. Ren, H.X. Bao, J.H. Gao, L.X. Zhang, Appl. Phys. Lett. **100**, 222910 (2012)
28. R.M. German, P. Suri, S.J. Park, J. Mater. Sci. **44**, 1–39 (2009)